Diagnosis, Prescription, and Prognosis of a Bell-State Filter by Quantum Process Tomography

M. W. Mitchell,[1] C. W. Ellenor,[1] S. Schneider,[2] and A. M. Steinberg[1]

[1]*Department of Physics, University of Toronto, 60 St. George Street, Toronto, Ontario, Canada M5S 1A7*

[2]*Chemical Physics Theory Group, Department of Chemistry, University of Toronto, 80 St. George Street, Toronto, Ontario, Canada M5S 3H6*

(Received 1 May 2003; published 19 September 2003)

We apply the techniques of quantum process tomography to characterize errors and decoherence in a prototypical two-photon operation, a singlet-state filter. The quantum process tomography results indicate a large asymmetry in the process and also the required operation to correct for this asymmetry. We quantify residual errors and decoherence of the filtering operation after this modification.

DOI: 10.1103/PhysRevLett.91.120402 PACS numbers: 03.65.Wj, 03.67.Mn, 03.67.Pp, 42.50.–p

Quantum computation promises exponential speedup in the solution of difficult problems such as factoring large numbers and simulating quantum systems [1,2]. In a quantum computer single- and multiple-qubit operations drive the system through a sequence of highly entangled states before the result is finally measured. A quantum computation is vulnerable to errors and to environmental decoherence, which destroys the entanglement. Characterization of quantum operations including errors and decoherence is a pressing issue for quantum information processing [3] and is possible by the technique of quantum process tomography (QPT) [4,5]. QPT has been demonstrated for single qubits [6,7] and for mixed ensembles of two-qubit systems [8] in NMR [9]. Here we present QPT of an entanglement-generating two-qubit operation, the partitioning of photons by a beam splitter in a Hong-Ou-Mandel (HOM) interferometer. Our characterization reveals large imperfections in the process and indicates the appropriate remedy. Finally, we extend the QPT results to predict the accuracy of the process, once repairs are carried out.

Multiqubit operations on photons, once thought to require very large optical nonlinearities, can now be performed with linear optical elements such as wave plates and beam splitters coupled with the highly nonlinear process of photodetection. This idea is exploited in schemes for linear optics quantum computation [10–12] and to generate multiphoton entangled states [13,14]. The schemes are probabilistic and employ postselection: the photodetection signals indicate when the correct operation has taken place. The HOM effect plays a central role in these proposals, and itself is a prototypical example of a postselected multiqubit operation: It generates correlations and entanglement without optical nonlinearities. The HOM effect has been used to produce entangled states for Bell inequality tests [15,16], to make probabilistic Bell-state measurements for quantum teleportation and entanglement swapping [17,18], and to test indistinguishability of consecutive photons from a single-photon source [19].

In the HOM effect, two photons meeting at a 50/50 beam splitter can leave by different output ports only if they are in some way distinguishable [20]. We use photon pairs which are indistinguishable in wavelength, spatial mode, and arrival time at the beam splitter, leaving only the polarization to (possibly) distinguish them. By detecting photons leaving from different output ports, we postselect an entangled polarization state. Ideally, the process acts as a filter for the Bell singlet state $\Psi^- = (HV - VH)/\sqrt{2}$, in which the photons have orthogonal polarizations in any basis. In any real apparatus this process includes errors and decoherence. Using the techniques of QPT, we determine how the polarization state, more specifically the 4×4 density matrix ρ which describes an arbitrary two-photon mixed state, changes in passing the beam splitter. In general, ρ will change as $\rho^{(\mathrm{in})} \rightarrow \rho^{(\mathrm{out})} = \mathcal{E}(\rho^{(\mathrm{in})})$, where $\mathcal{E}$ is the superoperator, a linear mapping from input density matrices to output density matrices. The superoperator completely characterizes the effect on the system, including coherent evolutions, decohering interactions with the environment, and loss.

We use a HOM interferometer constructed to produce arbitrary input polarizations and detect arbitrary output polarizations. The experimental setup is shown schematically in Fig. 1. A 7 mW beam of 351.1 nm light from an argon ion laser illuminates a pair of 0.6 mm thick β-barium borate crystals, cut for degenerate down-conversion at a half-opening angle of 3.3°. Pairs of down-conversion photons at 702.2 nm emerge from the crystals vertically polarized. This initial polarization state can be rotated into any input product state by the state preparation half- and quarter-wave plates immediately before the central beam splitter. The down-conversion beams meet the beam splitter at 45° incidence. The beam splitter itself [21] consists of a multilayer dielectric coating on a glass substrate, with an antireflection coated back face.

Polarization analyzers consisting of a quarter- and a half–wave plate before a polarizing beam splitter are used to select an arbitrary product state. Photons which

pass the analyzers are detected by single-photon counting modules and individual and coincidence detection rates are registered on a computer. Down-conversion beams were aligned to overlap both spatially and temporally on the beam splitter, giving a HOM dip visibility of $90\% \pm 5\%$ for both horizontal and vertical input polarizations. The process tomography measurements described below were performed at the center of this dip.

We prepare 16 linearly independent input states $\{\rho_i^{(\mathrm{in})}\}$ and measure the corresponding outputs $\{\rho_i^{(\mathrm{out})}\}$. The inputs [22] are the pure states $\rho_i^{(\mathrm{in})} = |\psi_i\rangle\langle\psi_i|$, where

$$\{\psi_1, \ldots, \psi_{16}\} = \{HH, HV, VV, VH, RH, RV, DV, DH, DR, DD, RD, HD, VD, VL, HL, RL\}, \quad (1)$$

and the polarizations are horizontal H, vertical V, diagonal $D = (H + V)/\sqrt{2}$, right circular $R = (H - iV)/\sqrt{2}$, and left circular $L = (H + iV)/\sqrt{2}$. A single output $\rho_i^{(\mathrm{out})}$ can be found by making projective measurements onto the 16 states $\{\psi_j\}$. The coincidence rates for these measurements are $R_{ij} = R_0 \mathrm{Tr}[\rho_i^{(\mathrm{out})}|\psi_j\rangle\langle\psi_j|]$, where R_0 is the constant rate of down-conversion at the crystals. Note that we use non-normalized output density matrices, i.e., $\mathrm{Tr}[\rho^{(\mathrm{out})}] \leq 1$, because photon pairs can be lost in the process. Absorption and scattering losses are small, but postselection necessarily removes a significant fraction of the pairs for most input states.

The measured coincidence rates R_{ij} are shown in Fig. 2. As expected for a filter, the output has similar polarization characteristics for all inputs, but not all are equally transmitted; e.g., HH and VV are blocked. A typical output density matrix, reconstructed using maximum-likelihood estimation [22] is shown in Fig. 3. The large coherence between HV and VH indicates that this is an entangled state, with a concurrence [22–24] of $C = 0.89$. The HOM effect is acting as an entangled-state filter, but the selected state is clearly not Ψ^-, which in this basis has a real density matrix and negative off-diagonal elements.

We can understand this behavior through the superoperator $\mathcal{E}$. For clarity, we work in the Bell-state basis $\{\Psi^-, \Psi^+, \Phi^-, \Phi^+\}$, where $\Psi^\pm = (HV \pm VH)/\sqrt{2}$ and $\Phi^\pm = (HH \pm VV)/\sqrt{2}$. We use a matrix representation for $\mathcal{E}$: The density matrix is written as a real 16-dimensional vector $\vec{\rho}$ made from the independent coefficients of the non-normalized density matrix, i.e., $\vec{\rho} = (\rho_{11}, \ldots, \rho_{44}, \mathrm{Re}[\rho_{12}], \mathrm{Im}[\rho_{12}], \mathrm{Re}[\rho_{13}], \ldots, \mathrm{Im}[\rho_{34}])^T$. The superoperator is represented by a matrix $\mathbf{M}$ which acts as

$$\vec{\rho}^{\,(\mathrm{out})} = \mathbf{M}\vec{\rho}^{\,(\mathrm{in})}. \quad (2)$$

In principle, $\mathbf{M}$ could be found from this equation by a simple inversion, since we measured R_{ij} for a basis set $\{\rho_i^{(\mathrm{in})}\}$. This procedure is sensitive to small errors and can produce a nonphysical $\mathbf{M}$, i.e., one which predicts nonphysical (mathematically, nonpositive semidefinite) $\rho^{(\mathrm{out})}$. Instead, we reconstruct $\mathbf{M}$ by maximum-likelihood estimation within the space of completely positive superoperators, i.e., operators that map physical density matrices to physical density matrices. Our reconstruction followed the formulation of Sudarshan *et al.* [25], although other

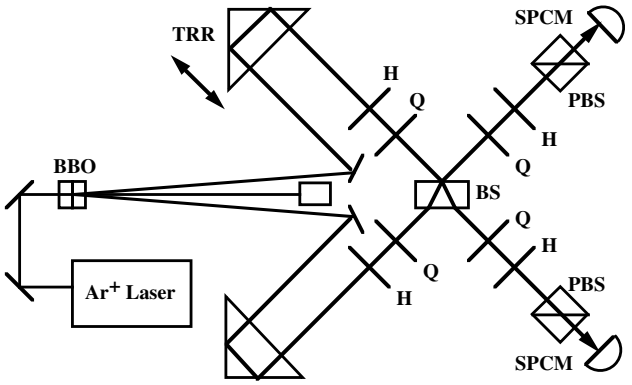

FIG. 1. Schematic of experimental setup. BBO: β-barium borate crystals, H: half-wave plate, Q: quarter-wave plate, BS: beam splitter, PBS: polarizing beam splitter, SPCM: single-photon counting module, and TRR: translatable retroreflector.

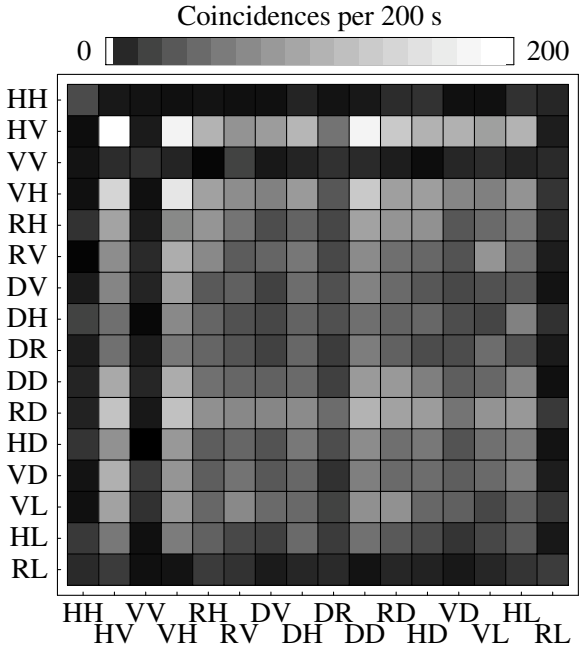

FIG. 2. Coincidence rates. Brightness indicates the count rate observed in a given two-photon polarization state (horizontal axis) for a given input polarization state (vertical axis).

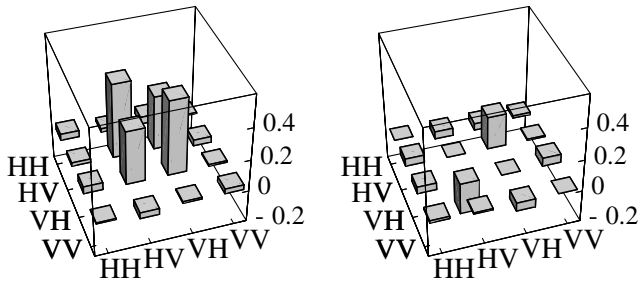

FIG. 3. Output density matrix (normalized) for an input state of HV. The left graph shows $\mathrm{Re}[\rho^{(\mathrm{out})}]$; the right graph shows $\mathrm{Im}[\rho^{(\mathrm{out})}]$.

reconstruction procedures may be more computationally efficient [26]. The reconstructed $\mathbf{M}$ is shown in Fig. 4(a), with error estimates from an ensemble of simulated data sets Poisson distributed around the measured data. This matrix is "normalized" to give $\mathrm{Tr}[\rho_{\mathrm{out}}] = 1/4$ when the input is a completely mixed state.

We verify the accuracy of the reconstructed superoperator using the input states LL and RR. These were not used in the reconstruction process and thus provide an independent test for systematic and statistical errors. These states are used as input, both to Eq. (2) and in the HOM interferometer. In both cases, prediction and the experimental result (again by maximum-likelihood reconstruction) agree with fidelity of 97%.

The superoperator $\mathbf{M}$ bears little resemblance to an ideal singlet-state filter, for which $M_{ij} = \delta_{i,1}\delta_{j,1}$. Clearly the process is not performing the intended filtering operation. In fact, it is nearly a projection onto a different maximally entangled state [27]. Written as a canonical Kraus operator sum [28,29], the superoperator allows us to find this state directly. In the sum $\mathcal{E}(\rho) = \sum_l \hat{K}_l \rho \hat{K}_l^\dagger$, the leading operator $\hat{K}_1$ is very nearly a projector onto the state $\Psi_\phi^- \equiv (HV - \exp[i\phi]VH)/\sqrt{2}$ with $\phi = 0.84\pi$. This immediately suggests a way to (partially) correct the behavior of the beam splitter. Adding a birefringent phase shifter which takes $VH \rightarrow \exp[-i\phi]VH$ before the beam splitter and the reverse operation afterward would give (nearly) a single-state filter.

Finally, we can predict the behavior if this correction were to be applied. The corresponding matrix $\mathbf{M}$ is shown in Fig. 4(b). The large $(1, 1)$ element indicates the filtering operation and the smaller nonzero elements contribute to decoherence and other errors. These errors presumably arise from imperfect overlap of the down–converted beams and residual imperfections in the beam splitter. They do not appear to have a simple form, but we can gain some insight from some simple measures, calculated using the superoperator. An unpolarized input (a completely mixed state) would give rise to an output that is 84% Ψ^-, or an average polarization ratio (intensity of Ψ^- versus average intensity of the other

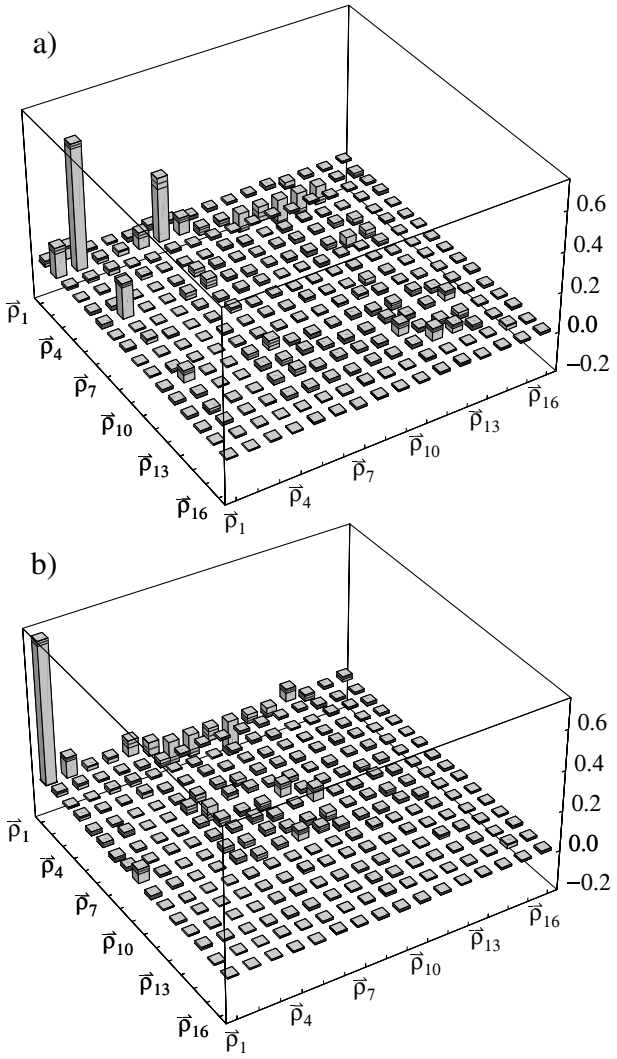

FIG. 4. Reconstructed superoperators for the postselected HOM process. (a) Superoperator as measured and (b) predicted superoperator after repair. The matrix $\mathbf{M}$ is shown, input density matrix elements at the bottom, output elements at the left, where the density matrices are represented in vector form (see text). Horizontal stripes on the vertical bars indicate the best estimated value and the statistical uncertainties.

three Bell states) of 16:1. This same output would be entangled, with a concurrence of $C = 0.70$. A concurrence of $C > 0$ is sufficient for a Bell inequality violation [30]. State purity can be quantified with the linear entropy $S_L \equiv 4/3(1 - \mathrm{Tr}[\rho^2])$ or the von Neumann entropy $S \equiv -\mathrm{Tr}[\rho \log_2 \rho]$. These entropy measures are zero for a pure state and 1 or 2, respectively, for a completely mixed two-qubit state. The corrected process would purify the mixed state from $S_L = 1$ to $S_L = 0.37$ ($S = 2$ to $S = 0.86$). We can also ask how well the repaired filter would maintain the coherence of an input. The pure input Ψ^- would be passed 75% of the time and emerge largely pure, with $S_L = 0.13$ ($S = 0.32$). The state Ψ^+ would be 13% passed with $S_L = 0.51$ ($S = 1.04$) and Φ^+, Φ^- would be passed

5% and 7% of the time with low purities of $S_L = 0.85$ and $S_L = 0.91$ ($S = 1.67$ and $S = 1.76$), respectively.

We have applied the techniques of quantum process tomography to a real-world Bell-state filter, implemented using the HOM effect and postselection. The QPT results reveal a large departure from ideal behavior, consistent with asymmetry in the HOM beam splitter. The QPT results also indicate the appropriate remedy and allow us to predict the behavior of the "fixed" Bell-state filter, including decoherence and residual errors. Further extensions of this first demonstration of two-photon quantum process tomography will allow us to study the feasibility of adaptively adjusting an error-avoidance scheme to react to the presence of a previously unknown source of noise. Such characterization techniques will be essential in the future development of quantum information processing, as the behavior of individual real-world systems will need to be understood in order to apply the methods of quantum error correction.

We thank Daniel Lidar, Jeff Lundeen, and Kevin Resch for assistance and helpful discussions. This work was supported by the National Science and Engineering Research Council of Canada, Photonics Research Ontario, the Canadian Institute for Photonic Innovations, and the DARPA-QuIST program (managed by AFOSR under Agreement No. F49620-01-1-0468).

[1] D. P. DiVincenzo, Science **270**, 255 (1995).
[2] A. Ekert and R. Jozsa, Rev. Mod. Phys. **68**, 733 (1996).
[3] Quantum information science and technology experts panel, "A Quantum Information Science and Technology Roadmap," 2002 (http://qist.lanl.gov).
[4] J. F. Poyatos, J. I. Cirac, and P. Zoller, Phys. Rev. Lett. **78**, 390 (1997).
[5] I. L. Chuang and M. A. Nielsen, J. Mod. Opt. **44**, 2455 (1997).
[6] F. De Martini, A. Mazzei, M. Ricci, and G. M. D'Ariano, quant-ph/0207143.
[7] J. B. Altepeter *et al.*, Phys. Rev. Lett. **90**, 193601 (2003).
[8] S. L. Braunstein *et al.*, Phys. Rev. Lett. **83**, 1054 (1999).
[9] A. M. Childs, I. L. Chuang, and D. W. Leung, Phys. Rev. A **64**, 012314 (2001).
[10] E. Knill, R. Laflamme, and G. J. Milburn, Nature (London) **409**, 46 (2001).
[11] J. D. Franson, M. M. Donegan, M. J. Fitch, B. C. Jacobs, and T. B. Pittman, Phys. Rev. Lett. **89**, 137901 (2002).
[12] A. Gilchrist, W.J. Munro, and A.G. White, quant-ph/0301112.
[13] P. Kok, H. Lee, and J. P. Dowling, Phys. Rev. A **65**, 052104 (2002).
[14] J. Fiurášek, Phys. Rev. A **65**, 053818 (2002).
[15] Z. Y. Ou and L. Mandel, Phys. Rev. Lett. **61**, 50 (1988).
[16] Y. H. Shih and C. O. Alley, Phys. Rev. Lett. **61**, 2921 (1988).
[17] D. Bouwmeester *et al.*, Nature (London) **390**, 575 (1997).
[18] J.-W. Pan, D. Bouwmeester, H. Weinfurter, and A. Zeilinger, Phys. Rev. Lett. **80**, 3891 (1998).
[19] C. Santori, D. Fattal, J. Vuckovic, G. S. Solomon, and Y. Yamamoto, Nature (London) **419**, 594 (2002).
[20] C. K. Hong, Z. Y. Ou, and L. Mandel, Phys. Rev. Lett. **59**, 2044 (1987).
[21] CVI Laser Corp. Nonpolarizing plate beam splitter BSNP-702.2-50-0525, 50% reflectance for both s and p polarizations at 702.2 nm.
[22] D. F. V. James, P. G. Kwiat, W. J. Munro, and A. G. White, Phys. Rev. A **64**, 052312 (2001).
[23] V. Coffman, J. Kundu, and W. K.Wootters, Phys. Rev. A **61**, 052306 (2000).
[24] W. K. Wootters, Phys. Rev. Lett. **80**, 2245 (1998).
[25] E. C. G. Sudarshan, P. M. Mathews, and J. Rau, Phys. Rev. **121**, 920 (1961).
[26] J. Fiurasek and Z. Hradil, Phys. Rev. A **63**, 020101 (2001).
[27] This may appear surprising, because it is well-known that the HOM effect must select Ψ^- if the beam splitter treats H and V polarizations symmetrically. But the beam splitter used here lacks inversion symmetry (only the front surface is reflective) and this allows a H/V asymmetry. Concretely, when both photons are reflected, one passes through the antireflection coated surface twice, while the other does not pass through it at all. If this coating is birefringent the inputs HV and VH will acquire different phase shifts upon double reflection. As a result, a different state within the $\{\Psi^-, \Psi^+\}$ subspace is selected. To our knowledge, this is the first observation of this asymmetry in the HOM effect.
[28] M. D. Choi, Linear Algebra Appl. **10**, 285 (1975).
[29] K. Kraus, *States, Effects, and Operations: Fundamental Notions of Quantum Theory* (Springer-Verlag, Berlin, 1983).
[30] F. Verstraete and M. M. Wolf, Phys. Rev. Lett. **89**, 170401 (2002).